Quantifying Sodium Dendrite Formation in $Na_5SmSi_4O_{12}$ Solid Electrolytes

Ansgar Lowack,* Yogeshbhai Nakum, Rafael Anton, Kristian Nikolowski, Mareike Partsch, and Alexander Michaelis

This study addresses the critical challenge in solid-state batteries (SSBs) by analyzing sodium dendrite formation in $Na_5SmSi_4O_{12}$ (NaSmSiO) solid electrolytes qualitatively and quantitatively. Symmetric Na|NaSmSiO|Na cells show negligible interfacial resistances and a high ionic conductivity of $(1.5 \pm 0.1)\,mS\,cm^{-1}$ at 30 °C with an activation energy for sodium transport of $(0.31 \pm 0.1)\,eV$. Dendrite formation is systematically induced using a linear current ramp of $1\,mA\,cm^{-2}\,h^{-1}$. Short circuits manifest as sharp resistance drops upon reaching the critical current density and are visually correlated with highly localized sodium filament penetration through the solid electrolyte. This observation indicates the presence of a "weakest link" within the material. The thermodynamics of this behavior are discussed. A statistical analysis of 30 cell tests reveals an average critical current density of $0.96\,mA\,cm^{-2}$. Failure occurrence is fitted to a shifted Weibull distribution. The resulting shape parameter of 1.10 suggests an approximately consistent failure rate above a critical threshold of $0.47\,mA\,cm^{-2}$. This work establishes quantitative benchmarks for NaSmSiO's dendrite resistance and introduces a robust statistical framework which can serve as a reference for future studies in this field.

1. Introduction

As global electrification advances, the importance of electrochemical energy storage technologies is increasing rapidly. Despite extensive research in the field, the development of rechargeable batteries without liquid components remains an elusive goal. Compared to contemporary lithium- or sodium-ion batteries, such solid-state batteries (SSBs) aim to substitute the liquid electrolyte with a solid electrolyte and the carbon-based electrode by a pure alkaline metal.

While the solid-state-battery concept promises advantages in terms of energy density, cycling stability, and safety compared to today's technology, it places high demand on the solid electrolyte and its interface with the alkaline metal electrode.[1–5] In principle, five key challenges need to be addressed: I) Conductivity of the solid electrolyte: The solid electrolyte must be comparable to liquid electrolytes in terms of lithium- or sodium-ion conductivity. Significantly lower conductivities will increase overall battery resistance and thus decrease energetic efficiencies due to Joule heating. II) Geometric interfacial contact: In the absence of liquid electrolytes, full geometric contact between the alkaline metal electrode and the solid electrolyte is far from guaranteed, due to high interfacial tensions between both components. As thoroughly discussed by Eckhardt et al.,[6,7] incomplete geometric contact between metal electrode and solid electrolyte will constrict the ionic current at the interface to points and surfaces of sufficiently good contact which can drastically increase cell resistance and local current density. III) Chemical interfacial stability: When good geometric contact is ensured, the solid electrolyte must be sufficiently inert against the highly reductive alkaline metals. If such decomposition reactions are neither thermodynamically nor kinetically hindered, they will result in a passivating interfacial layer and a drastic increase in cell resistance. IV) Delamination during sodium oxidation: When the alkaline metal electrode supplies ions to the solid electrolyte during discharge of the battery, each atom which is oxidized leaves a vacancy at the interface. If these vacancies are thermodynamically sufficiently stable and remain at the interface and if the current density and therefore the rate at which vacancies are created is too high, the vacancies can accumulate. The result is a delamination of the electrode which increases battery resistance.[8–11] Naturally, this phenomenon is closely linked to II. V) Dendrite formation during sodium reduction: If the alkaline metal ions are not reduced as a homogeneous layer on the alkaline metal electrode during battery charging, alkaline metal dendrites may form. These dendrites may penetrate the separator and short-circuit the battery. This issue is well known for alkaline metal electrodes in battery cells with liquid electrolytes and necessitated the invention of carbon-based electrodes.[12–14] Replacing the liquid electrolyte-drenched separator with a solid electrolyte does not inherently solve this issue.[15–22]

A. Lowack, A. Michaelis
Insitute of Materials Science
Dresden University of Technology
Helmholtzstraße 7, 01069 Dresden, Germany
E-mail: ansgar.lowack@ikts.fraunhofer.de

A. Lowack, Y. Nakum, R. Anton, K. Nikolowski, M. Partsch, A. Michaelis
Fraunhofer Institute for Ceramic Technologies and Systems (IKTS)
Winterbergstr. 28, 01277 Dresden, Germany

Batteries & Supercaps

Research Article
doi.org/10.1002/batt.202500279

Chemistry
Europe

European Chemical
Societies Publishing

Literature reviews indicate the extent to which different classes of solid electrolytes and alkaline metals address these challenges.[3,4,23,24] It is crucial to emphasize that for SSBs, sodium is more than a cheaper but inferior substitute for lithium. While sodium metal is a less potent reductive agent and has higher mass density, it is also softer and has lower yield strength compared to lithium metal.[25] This alone promises a significant advantage regarding challenges II and IV. Sodium might also be superior regarding the choice of suitable solid electrolytes: At a lithium conductivity of about $1\,mS\,cm^{-1}$ and a density of $5.1\,g\,cm^{-3}$, LLZO is the only known solid electrolyte with reasonable room temperature conductivity which is kinetically stable against lithium metal.[26–28] For sodium on the other hand, at least three promising candidates are known in beta-alumina, NASICON, and a group of glass-ceramics with the highly conductive crystalline phase $Na_5RSi_4O_{12}$ (R = Sc, Y, Lu, Tm, Er, Ho, Dy, Tb, Gd, Sm) that all outperform LLZO in terms of ionic conductivity and mass density.[29–32] In addition, beta-alumina and NASICON are known to be sufficiently stable against sodium metal.[8,33] The same is expected for $Na_5RSi_4O_{12}$, although definitive proof is still pending.

Therefore, meeting challenges I to IV might be possible in principle with LLZO for Li and beta-alumina, NASICON, or $Na_5RSi_4O_{12}$ for sodium. In addition, all four materials are rigid oxide ceramics with high strength and hardness—at least compared to other classes of solid electrolytes, such as thiophosphates, halides, or polymers—raising hopes that they might resist dendrite penetration (challenge V). Nevertheless, dendrites have been shown to penetrate all four materials.[34–36] While all five challenges are under active research, the issue of dendrite formation in solid electrolytes remains particularly poorly understood.

Most studies on the topic test dendrite formation in electrode-symmetric model cells with some variation of a DC-stripping/plating protocol. While this approach is close to the type of stress the interfaces would experience during cycling in the battery, the interfaces are subject to both reduction and oxidation of sodium; therefore, challenges IV and V are mixed at each interface. Dendrites could partially grow and then dissolve again until one dendrite penetrates the full separator and short circuits the cell. Furthermore, little research has been conducted on the statistics of dendrite formation. Rather, measurements on single cells are often examined to find a "critical current density" at which the cell fails due to dendrite formation. While this demonstrates the performance of a single cell, dendrite formation in ceramic solid electrolytes is likely linked to the mechanical properties of the ceramic. Since these properties inherently scatter between ceramic samples, due to the importance and the distribution of defects, a more quantitative evaluation is essential, as recently reported by QuantumScape for measurements on LLZO samples for lithium.[37]

This study aims to contribute to this understanding by qualitatively and quantitatively investigating sodium dendrite formation in the less well-known $Na_5SmSi_4O_{12}$ (NaSmSiO) solid electrolytes of the $Na_5RSi_4O_{12}$ type mentioned above. Samarium is selected because it is expected to widen the lattice more than smaller rare earth ions such as yttrium, thereby enhancing sodium mobility and ionic conductivity[38]—however, this hypothesis has yet to be definitively verified. To investigate dendrite formation symmetric Na|NaSmSiO|Na test cells were assembled and characterized using impedance spectroscopy. These cells then were subjected to a linearly increasing current to induce dendrite penetration of the separator. The nature of the dendrites during and after penetration was examined using optical microscopy. A quantitative testing protocol is proposed and demonstrated by forcing dendrite penetration in 30 identically assembled test cells and fitting the currents at which penetration occurred to a shifted Weibull distribution. The parameters of this distribution provide a more accurate measure of dendrite resistance compared to conventionally defined "critical current densities" for solid electrolytes.

2. Results and Discussion

2.1. Resistance of Model Cells

NaSmSiO is known to decompose upon exposure to air during sintering, resulting in the formation of a passivating layer.[36] Thus, as explained in the experimental section for symmetric Na|NaSmSiO|Na test cells, solid electrolyte pellets were sanded under inert conditions prior to contacting sodium on both sides of the pellet to remove such passivating layers and avoid their resistive effects.

While polishing the solid electrolyte surface is an intuitive approach to minimize surface defects and mitigate dendrite formation,[19] external pressures significantly greater than 20 MPa are necessary to achieve sufficiently good geometric contact between sodium metal and polished ceramic electrolytes.[39] Since such pressures could not be achieved with the setup used in this study, and because the exploration of methods to minimize dendrite formation is not the primary objective here, the NaSmSiO surfaces were left rough after sanding with P120 sandpaper. This approach has previously proven very effective in ensuring homogeneous intimate contact between alkaline metal and ceramic solid electrolyte.[39]

To verify the good Na|NaSmSiO contacts, temperature-dependent impedance spectra were recorded between −10 and 50 °C and fitted to an equivalent circuit, as exemplified in **Figure 1**a. Measurement frequency decreases from left to right in each spectrum. The experiment was conducted on three cells of identical assembly. Four contributions to the measured impedances are anticipated: A) At high frequencies, the resistance and polarization of the individual NaSmSiO grains can be expected. This process was observed by Wagner et al. for similar ionic conductors at frequencies above 1 MHz.[40] This frequency range has not been measured in this study and is not resolved in Figure 1a. The contribution is accommodated by an arial resistance R_A in the equivalent circuit; however, a precise evaluation of grain impedance would require impedance spectroscopy at frequencies above 1 MHz. B) Polarization of grain boundaries contributes at intermediate frequencies. This effect is attributed to the partially resolved semi-circles in the spectra of Figure 1a. The contribution is fitted by a parallel circuit of arial resistance R_B and constant
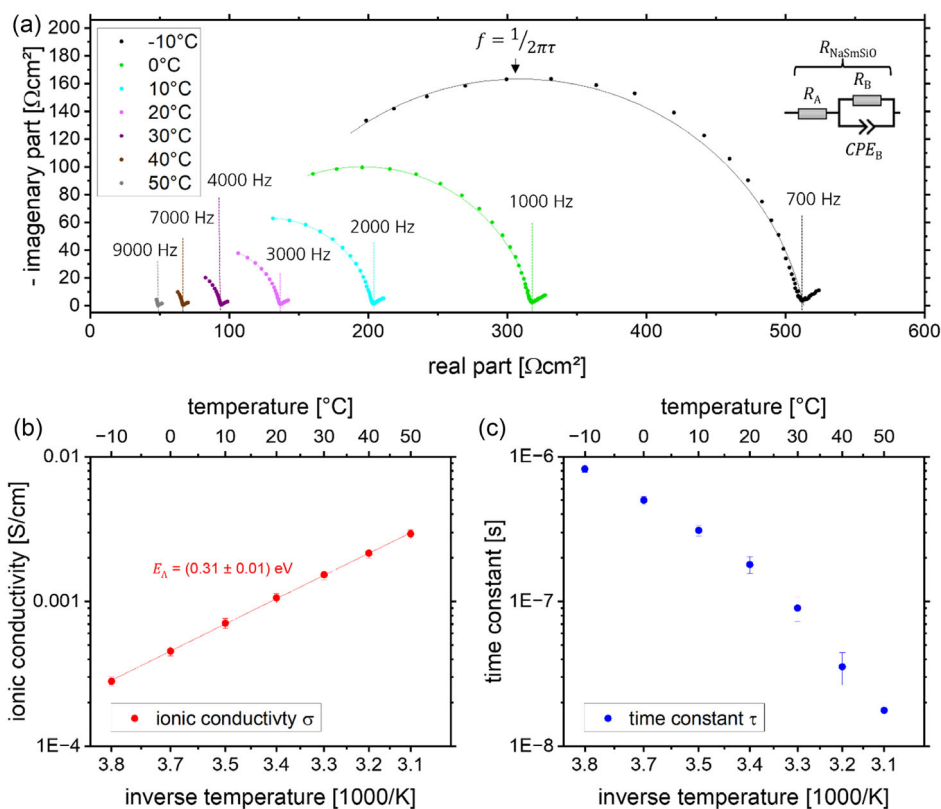
Figure 1. a) Impedance spectra of a Na|NaSmSiO|Na cell between −10 and 50 °C with inserted equivalent circuit. b) Average ionic conductivities of three test cells, fitted to the Arrhenius equation. c) Temperature-dependent time constant attributed to grain boundary polarization.

phase element CPE_B. C) At intermediate to low frequencies, pores at the Na|NaSmSiO interfaces will be polarized due to the dynamic current constriction as discussed by Eckhardt et al. No distinct semi-circle which could be assigned to this effect is found in the spectra.[7] This indicates homogenously intimate interfacial contact. D) At low frequencies, a slight increase in impedance is usually observed. Its origin is however not fully understood.[8,41] The phenomenon is observed below the frequencies indicated in Figure 1a and omitted from the fit.

In principle, additional resistivity due to a potential decomposition reaction of the NaSmSiO solid electrolyte in contact with metallic sodium might be expected at similar frequencies as contribution B. This was previously reported for the Li|LLZO and the Na|NASICON interface.[8,28] While the chemical stability of the Na|NaSmSiO interface is the subject of ongoing experimentation, no significant aging reaction in the hours after electrode contacting could be observed thus far that exceeds the temperature-dominated error of impedance measurements. The resistive effect of such an interfacial reaction on the time scale relevant for this study (hours) can therefore be considered insignificant compared to the influence of contribution B. Following this argumentation, the sodium ion conductivity of the solid electrolyte can be calculated from R_A and R_B. The ionic conductivity of ceramic ion conductors increases with temperature as described by the Nernst–Einstein relation, shifting the spectra to higher frequencies with temperature increases. The measurements are fitted to an Arrhenius equation to find the activation energy $E_A = (0.31 \pm 0.1)\,\Omega\,\text{cm}^2$ of ionic transport, using the equation

$$\sigma = \frac{d}{R_A + R_B} = \frac{A}{T}\exp\left(\frac{E_A}{k_B T}\right) \quad (1)$$

Here, d labels the thickness of the NaSmSiO sample and A a material-dependent constant. The results are plotted against temperature in Figure 1b. From R_B and the impedance

$$Z_{CPE}(f) = \frac{1}{Q(2\pi i f)^n} \quad (2)$$

of the constant phase element CPE_B at frequency f with fit parameters Q and n, the time constant of contribution B is calculated as

$$\tau = \sqrt[n]{QR_B} \quad (3)$$

and plotted against temperature in Figure 1c. In both Figure 1b, c, the results of the three cells are averaged. The average specific conductivity of $(1.5 \pm 0.1)\,\text{mS cm}^{-1}$ at 30 °C is similar to and in between the values reported by Schilm et al. and Anton et al. for the same solid electrolyte composition at the same temperature in measurement with blocking and certainly unreactive gold electrodes.[32,42] Consequently, the hypothesis that the Na|NaSmSiO interfaces do not contribute significantly to the resistivity of the model is supported. This indicates chemical interfacial stability and minimal interfacial current constriction. Hence, the cells appear well suited to study dendrite formation in electrochemical experiments. The phase purity of the NaSmSiO material was previously found to be 72.2 wt% of

Batteries & Supercaps

Research Article
doi.org/10.1002/batt.202500279

Chemistry Europe
European Chemical
Societies Publishing

the main crystalline phase $Na_5SmSi_4O_{12}$ and 27.0 wt% of the subphase $Na_{16.5}Sm_{2.5}Si_{12}O_{38}$, as discussed by Anton et al.[42]

2.2. Qualitative Investigation of Dendrite Formation

Failure of the Na|NaSmSiO interface can occur both during oxidation (i.e., "stripping") and reduction (i.e., "plating") of the sodium metal electrode. Failure during oxidation is commonly attributed to the accumulation of nanoscopic sodium voids at the interface, while failure during reduction is attributed to dendrite formation, that is, penetration of sodium metal filaments through the separator, leading to an electric short circuit of the electrolyte.

To provoke failure of the Na|NaSmSiO interface, a ramping current is driven through symmetric Na|NaSmSiO|Na cells at a slope of $1\,mA\,cm^{-2}\,h^{-1}$. The two modes of failure can be separated by adjusting the external pressure on the cell stack. As exemplary depicted in **Figure 2** in red, the current ramp at a low stack pressure of 0.1 MPa results in a sudden increase in cell resistance, most likely due to void formation driven delamination of the sodium electrode where sodium oxidation (i.e., "stripping") is taking place. This is followed by a short circuit and a sudden decrease in Ohmic voltage which is due to dendrite formation at the opposing electrode, as discussed in the following.

Void formation can be suppressed with a high enough external stack pressure as previously reported for Li|LLZO by Wang et al.[43] At an increased stack pressure of 10 MPa, the resulting current ramp indicates an approximately constant cell resistance until the cell short circuits, as depicted in green in Figure 2a. This type of short circuit is magnified for two further exemplary cells at 10 MPa of stack pressure in Figure 2b for the critical minutes before the voltage drop. In the cell depicted in green, voltage and resistance increase and then start dropping slowly from minute 40 onwards, until an abrupt short circuit occurs at minute 42. The cell depicted in blue showed a similar behavior in this current range. Here, the current was stopped as soon as the decreasing cell resistance became apparent and prior to the short circuit. This allows to investigate whether the decrease of cell resistance in the minutes before the short circuit can indeed be traced to dendrite propagation through the ceramic.

The short-circuited cells were then disassembled, the sodium electrodes removed, and the ceramic material sanded. Sodium dendrites are identified as gray filaments in the white ceramic material, as apparent from optical microscope images in **Figure 3**. Here, all shown samples were removed from cells to which the current was applied at 10 MPa of external stack pressure. Due to the low concentration of sodium metal, its quantitative verification was not feasible with X-ray diffraction (XRD). Qualitative confirmation was achieved by submerging the samples in water. Upon immersion, small bubbles formed at the filament, and the gray color faded, resulting in a once again white sample. This observation indicates the reaction of sodium metal with water, producing sodium hydroxide and hydrogen.

Figure 3a–c shows the top views of ceramics with completed short-circuit. The dendrites have a crack-like structure. Figure 3e is a cross section through the solid electrolyte pellet and the gray filament of the sample presented in Figure 3a. Figure 3e proves that these cracks run through the complete thickness of the NaSmSiO pellets, therefore explaining the short circuit. While in most samples only one single dendrite (like Figure 3a–c) is apparent, samples with two dendrites (Figure 3d) or even more prominent crack-like structures (Figure 3f) are observed too.

The cell whose current was stopped just before the electric short circuit (Figure 2b in blue) was analyzed in the same manner. **Figure 4** shows the resulting optical microscope image with two dendrites. Subsequently, the ceramic separator was gradually sanded down in layers of 100–250 μm and pictures of the two dendrites were taken at each depth. The depth resolution of the dendritic growth through the ceramic reveals the same crack-like shape of the dendrites as before. The crack width decreases with increasing depth. Neither dendrite completely penetrates the sample. The first dendrite extends ≈ 450 μm below the surface, while the second dendrite penetrates ≈ 1300 μm into the 1700 μm-thick NaSmSiO. In agreement with the observed voltage profile (Figure 2b, blue), it can be hypothesized that the second dendrite had almost arrived at the oxidizing electrode and the cell was stopped only seconds before the short circuit. Comparison with Figure 2b shows that with this specific testing protocol dendrites grow on a time scale of 1 min, once the dendrite starts to propagate.
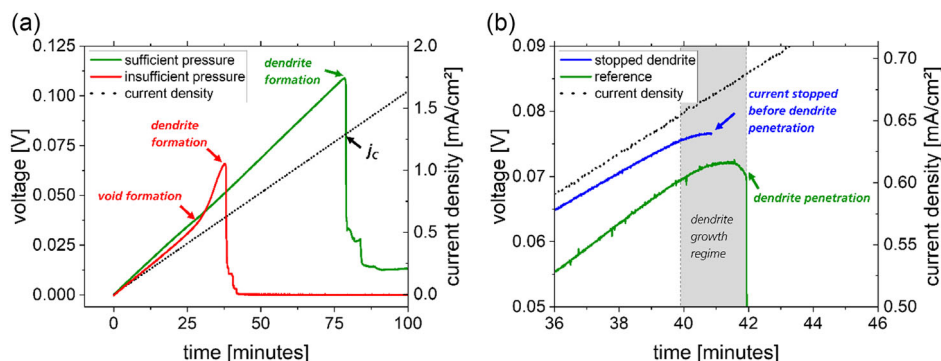

Figure 2. Voltage response of exemplary Na|NaSmSiO|Na cells to a ramping current. a) Shown in green is a cell at a stack pressure sufficient to suppress critical void formation (10 MPa) and exhibit approximately constant resistance until short circuit due to dendrite formation. Shown in red is a cell at a stack pressure insufficient to suppress critical void formation (0.1 MPa). Here cell resistance increases due to void formation before the resistance drops due to dendrite formation. b) Shown in blue is a cell which was stopped once cell resistance began to decrease; shown in green is a reference cell comparable to the green in (a), both cells at 10 MPa stack pressure.
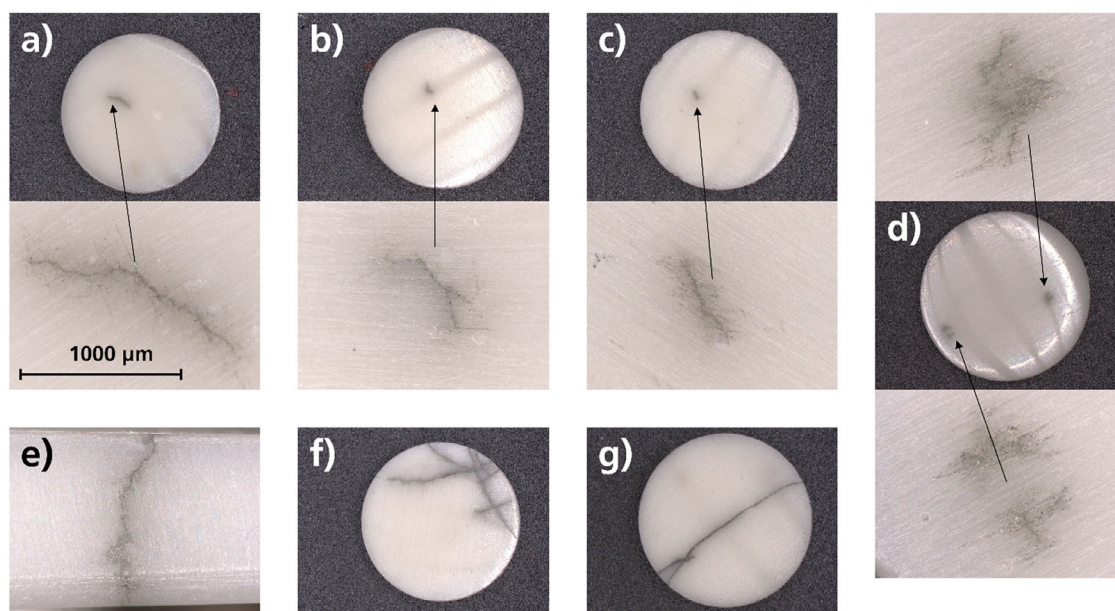
Batteries & Supercaps

Research Article
doi.org/10.1002/batt.202500279

Chemistry Europe
European Chemical
Societies Publishing

Figure 3. a–c) Typical top view of NaSmSiO pellets on the plating side after removal of the reducing sodium electrodes, prepared shortly after a short circuit occurred during current ramping. Dendrites are visible as gray filaments in the ceramic, as magnified. d) A sample with two dendrites. e) A cross section through the gray filament of the cell depicted in (a); the dendrite runs through the whole sample. f,g) Top views of the two cells that showed most deviation from the behavior depicted in (a–c). All pellets were taken from cells at 10 MPa of external stack pressure.
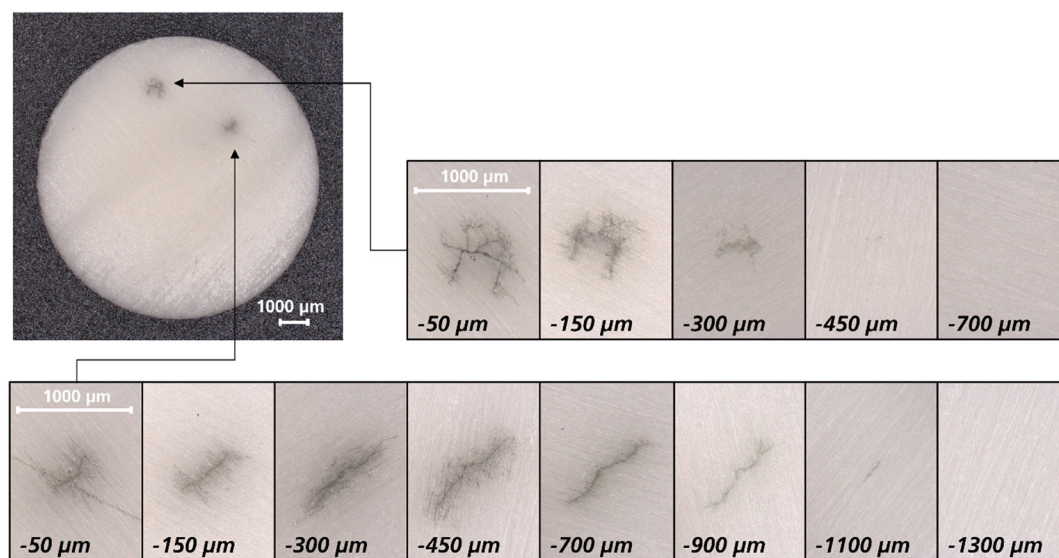

Figure 4. Top view of dendrites in a cell which was stopped during dendrite formation at 10 MPa of external stack pressure. Depicted are images at different depths below the previously removed electrode of sodium plating. Two dendrites are apparent that did not penetrate the sample completely.

The observation that the sodium dendrites are highly localized to a small area of the ceramic separator cannot be attributed to inhomogeneities in the interfacial contact between the sodium metal electrode and the ceramic separator. This conclusion is supported by the previously discussed negligible interfacial resistance, indicating minimal current constriction and a lack of significant heterogeneity in interfacial contact. Therefore, the localization of the dendrites likely arises from a weak link within the separator itself, potentially due to separator surface defects. Ning et al. provided a thorough analysis of dendrite nucleation at the interfaces between lithium metal electrodes and ceramic LPSCL solid electrolytes, emphasizing the influence of pores and microcracks near the interface.[19]

Using a similar reasoning, the behavior observed in Figure 3 and 4 may be explained by **Figure 5**. Here, a voltage U is applied between the sodium electrodes of the symmetric cell. The voltage is sufficient to drive a current of sodium ions from the bottom electrode (oxidation) to the upper electrode (reduction). Each sketch in Figure 5 emphasizes the morphology of pores and cracks at the interface between the solid electrolyte and the upper electrode, particularly one large pore in the middle of the upper electrode.
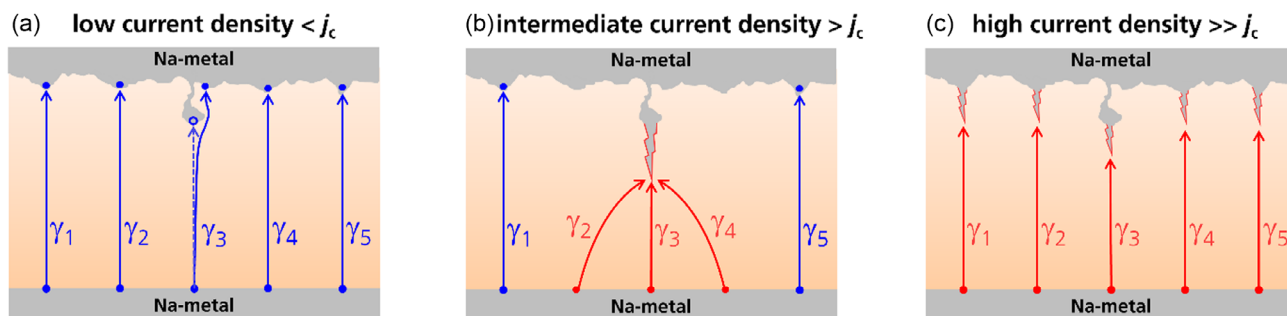
Batteries & Supercaps

Research Article
doi.org/10.1002/batt.202500279

Chemistry Europe
European Chemical
Societies Publishing

Figure 5. Model of dendrite penetration at different current densities. Blue conduction paths do not drive dendrite formation; red conduction paths do propagate dendrites. a) Low current density, no dendrite formation. b) Intermediate current density, dendrite formation at weakest link. c) High current density, dendrite formation at multiple sites.

All accessible pores and cracks of the separator that are connected to the upper electrode are filled with sodium metal—either due to sodium creep during pressurizing the freshly assembled cell or due to sodium plating at a subcritical current density. For simplification, the ceramics interface to the lower electrode is assumed to be homogeneous and smooth. This assumption is reasonable, since sodium metal is oxidized and no dendrites can nucleate there. Further, inhomogeneities in the electric field at the bottom interface will average out across the millimeter thickness of the separator. The latter exceeds the dimensions of both the grains and defects by far. Consequently, the current density at this bottom interface is approximately homogeneous.

Sodium atoms oxidized homogeneously at the bottom interface travel as ions along conduction paths, designated exemplary as γ_1 to γ_5 in Figure 5, toward the upper electrode where they are reduced back to sodium atoms. The work required to move the ion along any path γ_i contributes to Joule heating and is derived from Ohm's law as

$$Q_i(\gamma_i, \boldsymbol{j}) = e \int_{\gamma_i} \boldsymbol{E} \cdot d\boldsymbol{l} = e\rho \int_{\gamma_i} \boldsymbol{j} \cdot d\boldsymbol{l} \qquad (4)$$

with charge e of the sodium ion, electric field vector $\boldsymbol{E}$, current density vector $\boldsymbol{j}$, and specific resistance ρ of the solid electrolyte. The chemical energies required to oxidize the sodium atom and subsequently reduce the sodium ion cancel each other out, due to the symmetric nature of the electrodes. However, since all interfacial cracks and pores at the upper electrode are already filled with sodium, some mechanical energy

$$W_i = p_i V_{Na} \qquad (5)$$

is required to create space for the additional sodium atom. Here, V_{Na} is the molar volume of sodium, and p_i is the pressure needed to either displace other sodium ions or to propagate a crack in the solid electrolyte. This required pressure p_i strongly depends on where the additional sodium atom is deposited and on further assumptions: a) p_i is lowest and insignificant for conduction paths with deposition directly at the sodium electrode. There, any local pressure buildup would be instantaneously released into the vast electrode. Overall, the pressure buildup is balanced by the pressure release at the opposite sodium electrode. b) p_i is higher for sodium deposition at the tip of a sodium-filled pore or crack. It is

required to provide sufficient creep of the pre-existing sodium metal to push it out of the already filled pore or crack into the sodium electrode. p_i obviously depends on the shape of the pore or crack. It increases with the deposition rate. In an idealized scenario with an incompressible system and with the displacement of sodium governed by viscous flow through the crack, the initial pressure buildup scales approximately linearly with the deposition rate. c) Once p_i exceeds the pressure required to locally overcome the mechanical strength of the solid electrolyte, propagating a crack will become energetically favorable compared to pushing pre-existing sodium metal out of the pore or crack. As this crack propagation only depends on the mechanical strength of the solid electrolyte, it is independent of the deposition rate.

The actual conduction paths are found by minimizing energy and therefore by minimizing the voltage

$$U = \sum_i \frac{Q_i + W_i}{e} \qquad (6)$$

which is required to transport the ions from one electrode to the other. As explained above, heat Q_i always increases with current density and depends on the length of path γ_i, whereas work W_i depends on the local conditions at the end of path γ_i only and will only increase with current density until it reaches the threshold required to propagate the crack. This explains how dendrites are formed: 1) At initial voltages with current densities below some critical current density j_C, the volume work W_i will be insignificant for ions diffusing along paths γ_1, γ_2, γ_4, and γ_5 ending directly at the metal surface of the electrode (see a. above). The heat Q_1, Q_2, Q_4, and Q_5 will be minimized by minimizing the length of the corresponding conduction paths γ_1, γ_2, γ_4, and γ_5. These conduction paths thus will be approximately parallel to each other. In principle, the same applies for the shorter dotted path $\gamma_{3\text{-dotted}}$ shown in Figure 5a and thus the even lower $Q_{3-\text{dotted}}$. After an initial phase, work $W_{3-\text{dotted}}$ on the other hand is substantially higher than W_1, W_2, W_4, or W_5 if we assume (without restriction of generality) that work $W_{3-\text{dotted}}$ is due to a sodium creep out of the central pore into the electrode that is already restricted due to the pore's unfavorable geometry even at low current densities (see b. above). We further assume that the alternative work $W_{3-\text{dotted}}$ required to crack the solid electrolyte at the bottom

Batteries & Supercaps

Research Article
doi.org/10.1002/batt.202500279

Chemistry
Europe
European Chemical
Societies Publishing

of the central pore by a volume V_{Na} is even higher. In that case, due to the low current density, path γ_3 that circumvents the pore to reduce the ion directly at the electrode's surface is energetically preferred: The increase of $Q_{3-dotted}$ to Q_3 required to elongate path $\gamma_{3-dotted}$ to γ_3 will be overcompensated by the decrease of work $W_{3-dotted}$ to the insignificant work W_3. Consequently, no dendrites will form. Further, path $\gamma_{3-dotted}$ remains insignificant and is pursued only to the extent that the pressure in the pore is sustained. 2) At intermediate current densities above some critical current density j_C, the behavior changes. The work $W_{3-dotted}$ required for sodium creep out of the central pore into the electrode will have increased approximately linearly with current density. In contrast, alternative work $W_{3-dotted}$ required to crack the solid electrolyte at the bottom of the central pore by a volume V_{Na} has remained unchanged and now is lower than $W_{3-dotted}$ required for sodium creep. Now the increase of $Q_{3-dotted}$ to Q_3 required to elongate path $\gamma_{3-dotted}$ to γ_3 becomes larger than the difference of work $W_{3-dotted}$ (which is required to crack the solid electrolyte) to the insignificant work W_3. Consequently, it becomes energetically favorable to start propagating a dendrite at the bottom of the central pore, as shown in Figure 5b. The central pore thus acts as a weak link for dendrite formation, explaining the observed behavior in Figure 3 and 4. As the dendrite approaches the bottom electrode, more ions from the lower electrode will minimize Equation (6) by paying energy $W_{3-dotted}$ to deposit at the tip of the dendrite, propagating it further instead of traveling a longer conduction path of greater heat Q_i. This behavior is illustrated in Figure 5b for γ_2 and γ_4. Consequently, the dendrite propagates faster the deeper it penetrates. This explains the observation of a cascading voltage drop in Figure 2b (green).

The model also predicts another outcome, illustrated in Figure 5c: If the current density is not gradually increased but is instead instantly set to a value much larger than that required for dendrite propagation at the weakest link, Equation (1) becomes significantly larger than Equation (2). Additionally, the pressure needed for sufficient sodium creep to provide volume at the upper interface at this rate will exceed the pressure required to form cracks (i.e., to overcome the solid electrolyte's strength) across a wide range of defects, not just at the weakest links. Consequently, multiple dendrites will begin to propagate

and penetrate the sample rather than just one or two. This prediction was experimentally validated by preparing symmetric Na|NaSmSiO|Na cells at 10 MPa of external stack pressure which were subjected to a supercritical constant current density of 250 mA cm^{-2} for 4 s—more than two orders of magnitude higher than the current at which dendrites appeared in the ramp-type experiments (Figure 2). The transported charge of 1000 C cm^{-2} was approximately the same. The voltage response of the cells showed an almost instantaneous decrease in voltage, indicating rapid dendrite formation. An exemplary voltage profile can be found in Supporting Information S1. Impedance spectroscopy confirmed the occurrence of electron short circuits.

As before, the cells were disassembled, and the electrodes were removed. The appearance of the samples under the optical microscope is demonstrated in **Figure 6** for an exemplary sample. Figure 6a displays the side of the solid electrolyte separator where sodium was reduced, Figure 6b shows the side where sodium was oxidized, and Figure 6c depicts a cross section of the separator. A notably different type of dendritic penetration is observed compared to Figure 3 and 4. Instead of localized sodium penetration, the entire sample transitioned macroscopically from white to gray. In contrast to the observation in Figure 2, this happens on a time scale significantly faster than 1 min. Upon immersion in water, the sample returned to white while producing gas, confirming that sodium metal is responsible for the color change.

To ensure that the sodium filaments distributed throughout the sample volume did not result from a decomposition reaction of the NaSmSiO solid electrolyte due to the high voltage required for the 250 mA cm^{-2} supercritical current density, Cu|NaSmSiO|Cu cells with symmetric blocking electrodes were assembled and subjected to an 8 V voltage (which exceeds the current-driving voltage, see S1, Supporting Information) for 10 min. No discoloration of the white NaSmSiO was observed during this experiment. Thus, the gray discoloration observed in Figure 6 is a direct consequence of sodium transport through the solid electrolyte and must originate from the oxidized sodium metal electrode, confirming the behavior predicted in Figure 5c.

Following the thermodynamical considerations of Figure 5, dendrite suppression should increase when increasing the
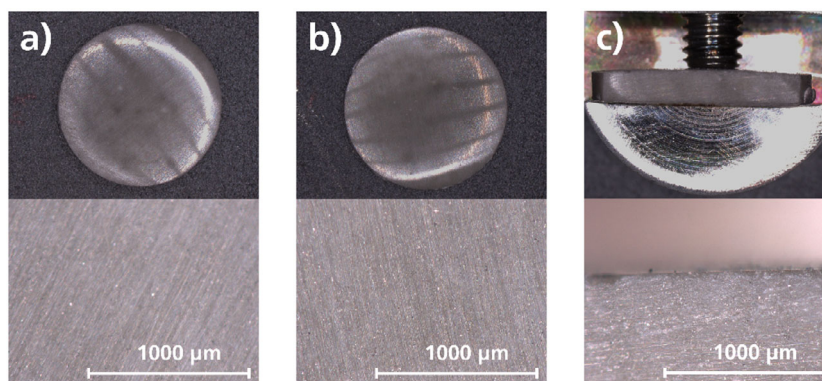

Figure 6. Top view of NaSmSiO pellets after removal of the reducing sodium electrodes, prepared after short circuit during supercritical current. The stripes are due to illumination. The whole sample is gray, as magnified. a) Viewed from the side at which sodium was reduced and b) oxidized. c) A cross section through the cell.

Batteries & Supercaps

Research Article
doi.org/10.1002/batt.202500279

Chemistry Europe
European Chemical
Societies Publishing

maximum value of Equation (5). This might be achieved by increasing the fracture toughness of the solid electrolyte directly (e.g., by using a different material), or by increasing its strength (e.g., by minimizing defect size, following Griffith's argumentation). This hypothesis should be tested in the future, once a quantitative measure of dendrite resistance is defined, as suggested in the following.

2.3. Quantitative Investigation of Dendrite Formation

A comparison of Figure 4 and 6 reveals that dendrite formation is significantly influenced by the experimental conditions used to promote their growth. Additionally, variability in dendrite formation across samples is anticipated, as dendrite formation is linked to crack propagation within the material. This crack propagation depends heavily on the distribution and shape of defects in the solid electrolyte and the interface. Therefore, assessing a material's resilience against dendrite formation is inherently complex.

To address this, a testing protocol is proposed involving a ramping current of $1\,\mathrm{mA\,cm^{-2}\,h^{-1}}$ applied to 30 symmetric Na|NaSmSiO|Na cells at a stack pressure of 10 MPa and 30 °C, as was previously exemplified in Figure 2. The resulting voltage profiles for all 30 samples are presented in Supporting Information S2 and S3.

From the data collected, the critical current density value j_c (at which dendritic short circuits occur) is extracted, as illustrated in Figure 2. The average of j_c is $0.96\,\mathrm{mA\,cm^{-2}}$. The set of these 30 j_c values is sorted into ten intervals and plotted as a histogram in **Figure 7**a (green). A shifted Weibull distribution is fitted to these j_c values and represented in Figure 7a (red) to determine its failure probability density function

$$P_f(j_c) = \begin{cases} 0, & \text{if } j < j_u \\ \frac{m}{j_0} \cdot \left(\frac{j_c - j_u}{j_0}\right)^{m-1} \cdot \exp\left(-\left(\frac{j_c - j_u}{j_0}\right)^m\right), & \text{if } j \geq j_u \end{cases} \tag{7}$$

The fit parameters are $j_u = 0.47\,\mathrm{mA\,cm^{-2}}$ (the threshold current below which no failures occurred), $j_0 = 0.51\,\mathrm{mA\,cm^{-2}}$ (normalization), and $m = 1.10$ (the Weibull or shape parameter). Using a shifted Weibull distribution is appropriate as it effectively

models various applications in material failure analysis, including mechanical failure in ceramics.

Following from Equation (7), the failure rate $R(j)$ at a current j is expressed as

$$R(j) = \frac{P_f(j)}{1 - \int_0^j P_f(j')dj'} = \begin{cases} 0, & \text{if } j < j_u \\ \frac{m}{j_0} \cdot \left(\frac{j - j_u}{j_0}\right)^{m-1}, & \text{if } j \geq j_u \end{cases} \tag{8}$$

Thus, for current densities above j_u, the Weibull parameter m indicates the following failure rate behaviors: 1) $m < 1$: decreasing failure rate with increasing current; 2) $m = 1$: constant failure rates with current, that is, random failures and an exponential distribution; and 3) $m > 1$: increasing failure rate with increasing current.

With $m = 1.10$, Equation (8) indicates a sharp increase in failure rate at $j = j_u$, followed by a gradual rise in failure rate at higher currents, as shown in Figure 7b. Therefore, based on this model, the probability of dendrite penetration through the solid electrolyte remains zero up to the critical current density j_u, after which it jumps to a finite value that remains relatively constant as current density increases.

A Kolmogorov–Smirnov test was conducted to assess the fit of the Weibull distribution (Equation (7)) to the $\{j_c\}$ dataset. Assuming the validity of Equation (7), the probability of observing a deviation between the measured data and the expected data that is at least as large as the one detected is 39%. This probability is considerably higher than conventional significance levels (e.g., 5%). Thus, the hypothesis of Equation (7) cannot be rejected and necessitates further validation.

Approximately one third of the cells exhibited minor increases in interfacial resistance before their short circuit (see S2, Supporting Information, with cells 4, 6, 8, 9, 13, 15, 17, 18, 19, 21, and 25), that is, with the current density increasing linearly over time, the voltage likewise increased linearly first and then increased faster. This most probably can be attributed to void formation at the oxidizing sodium electrode, which in turn is due to a major flaw in cell preparation: Sanding the surfaces of the solid electrolyte pellets manually leads to not perfectly plane-parallel opposite surfaces and thickness fluctuations. While the latter are small (<5% across the sample), they could cause drastic variations in interfacial pressure when the external pressure of
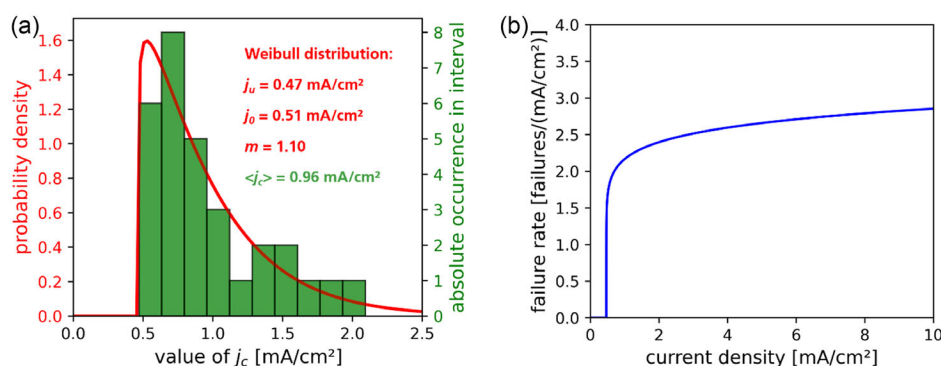

Figure 7. a) Histogram of current densities j_c at which short circuits occurred in 30 test cells. Values sorted into 10 intervals. Weibull distribution with parameters j_u, j_0, and m fitted to data set. b) Failure rate calculated from Weibull distribution.

Batteries & Supercaps

Research Article
doi.org/10.1002/batt.202500279

Chemistry Europe
European Chemical
Societies Publishing

10 MPa is applied perpendicular to the surfaces. Voids then probably form at areas of lower local pressure.

As the separator's thickness is significantly greater than the dimensions of these voids at the oxidizing sodium electrode, the electric field near the reducing interface would be minimally affected. Consequently, during dendrite nucleation at the reducing electrode interface, this influence is limited. With these considerations, it is valid to statistically analyze the j_c values from the 30 cells via Equation (7). However, the limited influence of pressure fluctuations might explain why the Kolmogorov–Smirnov hypothesis test yields a result of 39% only.

The question arises whether the behavior observed in Figure 7 correlates with the mechanical properties of the NaSmSiO solid electrolyte which are known to also follow a Weibull distribution. Fracture tests using the ball-on-three-ball method conducted on similarly prepared solid electrolyte pellets (with yttrium in place of samarium) by Wagner consistently resulted in Weibull modules m ranging from 3 to 9, depending on the composition.[44] This is notably higher than the $m = 1.10$ found in this study. However, the comparison is debatable since the ball-on-three-ball method forces critical crack growth, resulting in the complete fracture of the sample, while the dendrites observed in Figure 3 and 4 indicate a different behavior. The substrates are penetrated but not fractured which implies subcritical crack growth as the primary mechanism for penetration through the solid electrolyte. Hypothetically, the mechanical stress at the dendrite tip may be sufficient to locally surpass the material's strength. However, energy dissipation due to crack branching at grain boundaries results in sufficient energy dissipation to stop the crack from propagating significantly beyond the dendrite. A more direct comparison is needed to explore the relationship between mechanical and electrochemical failures during dendrite formation.

3. Conclusion

The central challenge of dendritic failure in SSBs was analyzed qualitatively and quantitatively by electrochemical impedance spectroscopy (EIS) of symmetric Na|NaSmSiO|Na cells. The cells exhibited immeasurably low interfacial resistances. NaSmSiO conductivities were at (1.5 ± 0.1) mS cm^{-1} at 30 °C. The activation energy for sodium transport was determined to be $E_A = (0.31 \pm 0.1)$ eV in temperature-dependent EIS measurements. Therefore, NaSmSiO holds great promise as a solid electrolyte in direct contact with sodium metal.

Dendrite formation in the symmetric cells was tested by applying a linearly increasing current at a rate of 1 mA cm^{-2} h^{-1}. Sudden drops in internal cell resistance were observed and correlated with dendrite formation. The dendrites manifested as highly localized sodium filaments within the solid electrolyte. This indicates that dendrite formation occurs at some type of weakest link in the samples. This behavior was thermodynamically discussed based on previous reports[19] on the central role of surface morphology on dendrite nucleation by qualitatively comparing the work required to deposit sodium at the tip of a dendrite and the Joule heating cost associated with the length

of the conduction path in dependence of current density. It is predicted that increasing fracture toughness should increase the resilience to dendrite penetration.

To quantify dendrite formation, 30 symmetric Na|NaSmSiO|Na cells were subjected to a linearly increasing current until dendrite penetration occurred. Consistent with failure analysis practices, the distribution of critical current densities was fitted to a shifted Weibull distribution. A Kolmogorov–Smirnov test confirmed that the measured data did not significantly deviate from this model. None of the cells failed at current densities below $j_u = 0.47$ mA cm^{-2}, with an average critical current density of $\langle j_c \rangle = 0.96$ mA cm^{-2}. The obtained Weibull (shape) parameter $m = 1.10$ suggests an approximately constant failure rate, independent of current density, above the threshold $j_u = 0.47$ mA cm^{-2}. This highlights that the inherent property scattering of ceramic materials extends to dendrite formation, underscoring the necessity of statistical testing with sufficient sample sizes rather than relying on a limited number of tests. It is recommended to utilize the j_u value, below which dendrite formation is not observed in a sufficient number of cells, to quantify dendrite formation for a specific solid electrolyte.

Following Weibull's arguments regarding the fracture statistics of ceramic mechanical properties, it is hypothesized that reducing the scattering of the size of the largest defect responsible for the weakest link in dendrite formation will decrease the scattering of dendrite formation between samples and increase m. Future experiments could explore how variations in ceramic microstructures influence the Weibull parameter m, to gain insights into the nature of the defects responsible for dendrite formation. Also, the method should be applied to quantify dendrite formation in other solid electrolytes such as NASICON or LLZO to confirm that the given argumentation is indeed universal to brittle ceramic ion conductors.

4. Experimental Section

Electrolyte and Cell Preparation

The solid electrolyte pellets were prepared following the listed steps: 1) Powder synthesis: Raw materials Na$_2$CO$_3$ (AnalaR NORMAPUR, VWR), SiO$_2$ (Millisil W8, Quarzwerke Frechen, Germany), and Sm$_2$O$_3$ (Alfa Aesar, Kandel, Germany) were blended in a tumble mixer (TURBULA, Willy A. Bachofen AG, Muttenz, Switzerland) for 30 min, maintaining a molar ratio of 35.7:57.1:7.2 (Na$_2$CO$_3$:SiO$_2$:Sm$_2$O$_3$), corresponding to the desired Na$_5$SmSi$_4$O$_{12}$ composition. The resulting powder mixture was melted in a platinum crucible at 1350 °C for 1 h, followed by quenching on a brass block. The glass frits produced were milled using a disc mill (RS1, Retsch, Germany) and then subjected to 12 h of milling in a planetary ball mill (Pulverisette 5, FRITSCH, Germany). Subsequently, the milled powders were calcined at 950 or 1100 °C in ambient atmosphere for 1 h to facilitate the crystallization of the amorphous precursor powders into Na$_5$SmSi$_4$O$_{12}$ powders. Finally, these precrystallized powders were further milled in an attritor mill (NETZSCH-Feinmahltechnik GmbH, Germany) for 1 h at 1000 rpm. 2) Preparation of samples before sintering: 0.5 g of the NaSmSiO-powder was pressed in a stainless-steel tool under argon at a uniaxial pressure of 30 MPa to pellets of 12 mm diameter and a thickness of 3 mm. 3) Sintering: Green pellets were transferred

Batteries & Supercaps

Research Article
doi.org/10.1002/batt.202500279

Chemistry Europe
European Chemical
Societies Publishing

to an air-vented Muffle-furnace (RWF 1200, Carbolite Gero GmbH & Co. KG, Germany) and heated to 1050 °C at a rate of 3 °C min^{-1}, sintered at 1050 °C for 1 h, and subsequently thermalized to room temperature at 3 °C min^{-1}. Sintered samples had a diameter of 10 mm. 4) Preparation of sintered samples: Sintered electrolyte pellets were transferred to an argon-filled glovebox after sintering. The samples were annealed at 700 °C for 2 h in argon atmosphere to remove potential surface layers of Na_2CO_3 (muffle furnace inside the glovebox) and sanded from both sides (SiC-sanding paper; P120 grit), to a thickness of (1.8 ± 0.1) mm. 5) Sodium metal electrodes: NaSmSiO-pellets were sandwiched between two sodium foils and pressed at 10 MPa and 97 °C in a heated press inside the glovebox. 6) Test cell assembly: Cell stacks were sealed in Pat-Force-Cells (EL-Cell GmbH) at an external stack pressure of 0.1 or 10 MPa.

Electrochemical Measurements

The assembled test cells were transferred to a temperature chamber, connected to a Biologic VMP3 Potentiostat, and thermalized for 2 h. Three types of electrochemical measurement were conducted in this study, always with a four-wire-setup: 1) EIS: To determine the resistance contributions of the cells, impedance spectra between 1 MHz and 10 Hz were recorded between (-10 ± 1) and (50 ± 1) °C at 10 mV voltage amplitude. Due to cable impedance contribution, measurements above 0.8 MHz were omitted. 2) Current-dependent dendrite testing: To investigate dendrite formation at the sodium-reducing interface and to find the current density at which dendrites appear, a ramping current density at a slope of 1 mA cm^{-2} h^{-1} (normalized to the area of the cells' cross section) was applied at (30 ± 1) °C. During the measurement, the voltage was recorded. 3) Over-critical dendrite testing: To investigate the reaction of the solid electrolyte to currents which are above any critical current density, a constant 250 mA cm^{-2} current density was applied.

Postmortem Analysis of Short-Circuited Cells

To investigate the nature of dendrite growth in the solid electrolyte, cells with short circuits were transferred back to the glovebox and disassembled. The Na|NaSmSiO|Na cell stack was taken out of the cell housing. The electrodes were removed with a scalpel and SiC sanding paper of grits ranging from P120 to P2500. Pictures were taken with a (VHX-970F/970FN) optical microscope inside the glovebox. To get depth resolution, the penetrated separators were gradually sanded down in between pictures.

Data Analysis

A python program was used for the quantitative evaluation of the dendrite tests. Fit parameters of Equation (7) are determined using a maximum likelihood estimation (MLE) on the datapoints in Table S1, Supporting Information, by defining the Log-Likelihood-function for Equation (7) and using the "minimize" function of the python library scripy.optimize. The Kolmogorov–Smirnov test was carried out using the function "ks_2samp" of the python library scipy.stats.

Acknowledgements

Conflict of Interest

The authors declare no conflict of interest.

Author Contributions

Ansgar Lowack: designed the experiments. **Rafael Anton, Ansgar Lowack**, and **Yogeshbhai Nakum**: prepared the solid electrolyte pellets. **Ansgar Lowack** and **Yogeshbhai Nakum**: prepared all cells and performed the experiments. **Ansgar Lowack**: evaluated the data and wrote the manuscript. All authors discussed the results and contributed to the preparation of the manuscript.

Data Availability Statement

The data that support the findings of this study are available from the corresponding author upon reasonable request.

[1] C. Heubner, S. Maletti, H. Auer, J. Hüttl, K. Voigt, O. Lohrberg, K. Nikolowski, M. Partsch, A. Michaelis, *Adv. Funct. Mater.* **2021**, *31*, 2100123.
[2] M. Rosner, S. Cangaz, A. Dupuy, F. Hippauf, S. Dörfler, T. Abendroth, B. Schumm, H. Althues, S. Kaskel, *Adv. Energy Mater.* **2025**, *15*, 2404790.
[3] A. Joshi, D. K. Mishra, R. Singh, J. Zhang, Y. Ding, *Appl. Energy* **2025**, *386*, 125546.
[4] J. Janek, W. G. Zeier, *Nat. Energy* **2023**, *8*, 230.
[5] L. Xu, S. Tang, Y. Cheng, K. Wang, J. Liang, C. Liu, Y.-C. Cao, F. Wei, L. Mai, *Joule* **2018**, *2*, 1991.
[6] J. K. Eckhardt, S. Kremer, L. Merola, J. Janek, *ACS Appl. Mater. Interfaces* **2024**, *16*, 18222.
[7] J. K. Eckhardt, P. J. Klar, J. Janek, C. Heiliger, *ACS Appl. Mater. Interfaces* **2022**, *14*, 35545.
[8] T. Ortmann, S. Burkhardt, J. K. Eckhardt, T. Fuchs, Z. Ding, J. Sann, M. Rohnke, Q. Ma, F. Tietz, D. Fattakhova-Rohlfing, C. Kübel, O. Guillon, C. Heiliger, J. Janek, *Adv. Energy Mater.* **2023**, *13*, 2302729.
[9] P. Barai, T. Fuchs, E. Trevisanello, F. H. Richter, J. Janek, V. Srinivasan, *Chem. Mater.* **2024**, *36*, 2245.
[10] Y. Lu, C.-Z. Zhao, J.-K. Hu, S. Sun, H. Yuan, Z.-H. Fu, X. Chen, J.-Q. Huang, M. Ouyang, Q. Zhang, *Sci. Adv.* **2022**, *8*, eabn5097.
[11] Z. Tang, A. Morchhale, J. R. Sayre, J.-H. Kim, *J. Energy Storage* **2025**, *107*, 114966.
[12] Z. Li, J. Huang, B. Y. Liaw, V. Metzler, J. Zhang, *J. Power Sources* **2014**, *254*, 168.
[13] X. Zhang, A. Wang, X. Liu, J. Luo, *Acc. Chem. Res.* **2019**, *52*, 3223.
[14] A. Yoshino, *Nobel Lecture in Chemistry* **2019**. Press release. NobelPrize.org. Nobel Prize Outreach 2025.
[15] J. A. Lewis, S. E. Sandoval, Y. Liu, D. L. Nelson, S. G. Yoon, R. Wang, Y. Zhao, M. Tian, P. Shevchenko, E. Martínez-Pañeda, M. T. McDowell, *Adv. Energy Mater.* **2023**, *13*, 2204186.
[16] B. G. Choobar, H. Hamed, S. Yari, M. Safari, *ChemElectroChem* **2024**, *11*, e202300456.
[17] L. Geng, D. Xue, J. Yao, Q. Dai, H. Sun, D. Zhu, Z. Rong, R. Fang, X. Zhang, Y. Su, J. Yan, S. J. Harris, S. Ichikawa, L. Zhang, Y. Tang, S. Zhang, J. Huang, *Energy Environ. Sci.* **2023**, *16*, 2658.
[18] H. Liu, X.-B. Cheng, J.-Q. Huang, H. Yuan, Y. Lu, C. Yan, G.-L. Zhu, R. Xu, C.-Z. Zhao, L.-P. Hou, C. He, S. Kaskel, Q. Zhang, *ACS Energy Lett.* **2020**, *5*, 833.
[19] Z. Ning, G. Li, D. L. R. Melvin, Y. Chen, J. Bu, D. Spencer-Jolly, J. Liu, B. Hu, X. Gao, J. Perera, C. Gong, S. D. Pu, S. Zhang, B. Liu, G. O. Hartley, A. J. Bodey, R. I. Todd, P. S. Grant, D. E. J. Armstrong, T. J. Marrow, C. W. Monroe, P. G. Bruce, *Nature* **2023**, *618*, 287.

[20] H. Sun, A. Celadon, S. G. Cloutier, K. Al-Haddad, S. Sun, G. Zhang, *Battery Energy* **2024**, *3*, 20230045.

[21] A. V. Virkar, L. Viswanathan, *J. Am. Ceram. Soc.* **1979**, *62*, 528.

[22] Z. Yu, X. Zhang, C. Fu, H. Wang, M. Chen, G. Yin, H. Huo, J. Wang, *Adv. Energy Mater.* **2021**, *11*, 2003250.

[23] M. Ma, M. Zhang, B. Jiang, Y. Du, B. Hu, C. Sun, *Mater. Chem. Front.* **2023**, *7*, 1268.

[24] H. Si, J. Ma, X. Xia, Q. Wang, S. Geng, L. Fu, *Chemistry* **2025**, *31*, e202403247.

[25] M. J. Wang, J.-Y. Chang, J. B. Wolfenstine, J. Sakamoto, *Materialia* **2020**, *12*, 100792.

[26] R. Murugan, V. Thangadurai, W. Weppner, *Angew. Chem., Int. Ed.* **2007**, *46*, 7778.

[27] C. Wang, K. Fu, S. P. Kammampata, D. W. McOwen, A. J. Samson, L. Zhang, G. T. Hitz, A. M. Nolan, E. D. Wachsman, Y. Mo, V. Thangadurai, L. Hu, *Chem. Rev.* **2020**, *120*, 4257.

[28] T. Krauskopf, B. Mogwitz, H. Hartmann, D. K. Singh, W. G. Zeier, J. Janek, *Adv. Energy Mater.* **2020**, *10*, 2000945.

[29] M. P. Fertig, K. Skadell, M. Schulz, C. Dirksen, P. Adelhelm, M. Stelter, *Batteries Supercaps* **2022**, *5*, e202100345.

[30] Q. Ma, F. Tietz, *ChemElectroChem* **2020**, *7*, 2693.

[31] B. A. Maksimov, Y. A. Kharitonov, N. V. Belov, *Dokl. Akad. Nauk SSSR* **1973**, *210*, 123.

[32] J. Schilm, R. Anton, D. Wagner, J. Huettl, M. Kusnezoff, M. Herrmann, H. K. Kim, C. W. Lee, *Materials* **2022**, *15*, 4567.

[33] R. O. Ansell, *J. Mater. Sci.* **1986**, *21*, 365.

[34] C. Zhu, T. Fuchs, S. A. L. Weber, F. H. Richter, G. Glasser, F. Weber, H.-J. Butt, J. Janek, R. Berger, *Nat. Commun.* **2023**, *14*, 1300.

[35] L. Liu, Q. Ma, X. Zhou, Z. Ding, D. Grüner, C. Kübel, F. Tietz, *J. Power Sources* **2025**, *626*, 235773.

[36] J. Hüttl, W. Cai, D. Wagner, J. Schilm, M. Kusnezoff, K. Nikolowski, N. Shaji, C. W. Lee, M. Partsch, A. Michaelis, *Solid State Ionics* **2022**, *376*, 115856.

[37] D. M. Gendron, A. Torabi, M. Wanees, M. S. Dsouza, B. Feddersen, T. Holme, *J. Electrochem. Soc.* **2025**, *172*, 020511.

[38] R. D. Shannon, B. E. Taylor, T. E. Gier, H. Y. Chen, T. Berzins, *Inorg. Chem.* **1978**, *17*, 958.

[39] A. Lowack, P. Grun, R. Anton, H. Auer, K. Nikolowski, M. Partsch, M. Kusnezoff, A. Michaelis, *Batteries Supercaps* **2024**, *7*, e202300567.

[40] D. Wagner, M. Kusnezoff, J. Schilm, C. Heubner, M. Herrmann, A. Weber, P. Braun, C. W. Lee, N. Shaji, *J. Eur. Ceram. Soc.* **2022**, *42*, 3939.

[41] T. Ortmann, T. Fuchs, J. K. Eckhardt, Z. Ding, Q. Ma, F. Tietz, C. Kübel, M. Rohnke, J. Janek, *Adv. Energy Mater.* **2024**, *14*, 2302729.

[42] R. Anton, A. Lowack, D. Wagner, J. Schilm, M. Kusnezoff, *J. Eur. Ceram. Soc.* **2025**, *45*, 117163.

[43] M. J. Wang, R. Choudhury, J. Sakamoto, *Joule* **2019**, *3*, 2165.

[44] D. Wagner, Dissertation, TU Dresden **2022**.